JTTEE5 10:584-591

Process Study, Microstructure, and Matrix Cracking of SiC Fiber Reinforced $MoSi_2$ Based Composites

Kyeong Ho Baik and Patrick S. Grant

(Submitted 5 October 2000; in revised form 18 December 2000)

SiC fiber reinforced SiAlON-$MoSi_2$ composites have been manufactured by a concurrent fiber winding and low pressure plasma spraying (LPPS) technique to produce a multilayer, circumferentially fiber reinforced composite ring. The LPPS parameters for SiAlON-$MoSi_2$ powder were optimized by a two-level experimental design approach followed by further optimization, which provided a smooth sprayed surface, low matrix porosity, and high deposition efficiency. The microstructure of SiAlON-$MoSi_2$ matrix consisted of a lamellar structure built up of individual splats and a uniform distribution of discontinuous SiAlON splats throughout the $MoSi_2$ matrix. The spray/wind composites exhibited 2% porosity and well-controlled fiber distribution. High temperature consolidation led to the formation of a thick reaction zone at the fiber-matrix interface by a chemical reaction between C coating and $MoSi_2$. Matrix cracking occurred in SiC_f (15 vol.%)/$MoSi_2$ after cooling from 1500 to 25 °C and was attributed to the large tensile residual stresses in the matrix developed on cooling because of coefficient of thermal expansion (CTE) mismatch between matrix and fiber. The addition of 40 vol.% SiAlON into the $MoSi_2$ effectively eliminated the matrix cracking by reducing the matrix-fiber CTE mismatch. Predictions of matrix cracking stress on the basis of residual stresses in the composites showed that the maximum permissible fiber volume fraction to avoid matrix cracking was 6% for SiC_f/$MoSi_2$ and 23% for SiC_f/SiAlON(40 vol.%)-$MoSi_2$.

Keywords chemical reaction, low pressure plasma spraying, matrix cracking, molybdenum disilicide, SiC fiber

1. Introduction

$MoSi_2$ is a candidate material for future high temperature structural applications and a potential competitor to both current superalloys and other advanced materials because of the attractive combination of excellent elevated temperature oxidation resistance, high melting point (2030 °C), good thermal conductivity (30 W/mK above 1000 °C), and moderate density (6.24 g/cm^3).[1] Unfortunately, $MoSi_2$ is brittle at low temperatures, has a high creep rate at elevated temperatures above 1200 °C, and suffers accelerated oxidation at intermediate temperatures of 400 to 500 °C (pesting).[1–7]

In the last decade, research efforts have been aimed at improving the mechanical properties of $MoSi_2$, particularly with regard to low-temperature fracture toughness and high-temperature creep resistance through solid-solution alloying, particulate/whisker reinforcement, and fiber reinforcement.[2–6] A substantial improvement in the properties of $MoSi_2$ is expected by reinforcing with continuous SiC fiber. However, coefficient of thermal expansion (CTE) mismatch between SiC (4.5×10^{-6}/ °C) and $MoSi_2$ (8.3×10^{-6}/ °C) leads to large residual stresses generated on cooling from a high processing temperature of up to 1500 °C, resulting in an extensive matrix cracking during manufacture by hot pressing. Recently, it has been reported that the addition of Si_3N_4 particles led to a reduction in the CTE of the $MoSi_2$ matrix and, thus, eliminated matrix cracking in SiC reinforced composites manufactured by a powder cloth and hot press method.[7] Atmospheric plasma spraying (APS) as a means of manufacturing SiC fiber reinforced $MoSi_2$ composite monotape has recently been demonstrated by a collaboration between Oxford University (Wellington Square, Oxford, United Kingdom) and Los Alamos National Laboratory (Los Alamos, NM).[8] However, matrix cracking and fiber damage occurred during/after APS in this preliminary study because of nonoptimized processing conditions.

The objective of the present study is to explore the use of the low pressure plasma spraying (LPPS) for manufacturing multilayer SiC fiber reinforced $MoSi_2$ based composites for ring or tube components in a single spraying operation. Premixed SiAlON-$MoSi_2$ powder is used as the matrix to lower the matrix CTE (SiAlON CTE $\sim 3.5 \times 10^{-6}$/ °C[9]). The LPPS parameters for $MoSi_2$-SiAlON powder are optimized in order to achieve a smooth sprayed surface, low matrix porosity, and best deposition efficiency. The microstructures of matrix and composite, particularly interfaces of SiAlON-$MoSi_2$ and SiC_f-$MoSi_2$, are examined. The matrix cracking stress is predicted as a function of matrix CTE and fiber diameter and provides an estimate of maximum fiber volume fraction permitted to avoid matrix cracking.

2. Experimental Procedure

2.1 Materials

Forty volume percent SiAlON added $MoSi_2$ feedstock powder was prepared from commercially available $MoSi_2$ and

Kyeong Ho Baik and Patrick S. Grant, Oxford Centre for Advanced Materials and Composites, Department of Materials, University of Oxford, Oxford OX1 3PH, United Kingdom. Contact e-mail: kyeong.baik@materials.ox.ac.uk.

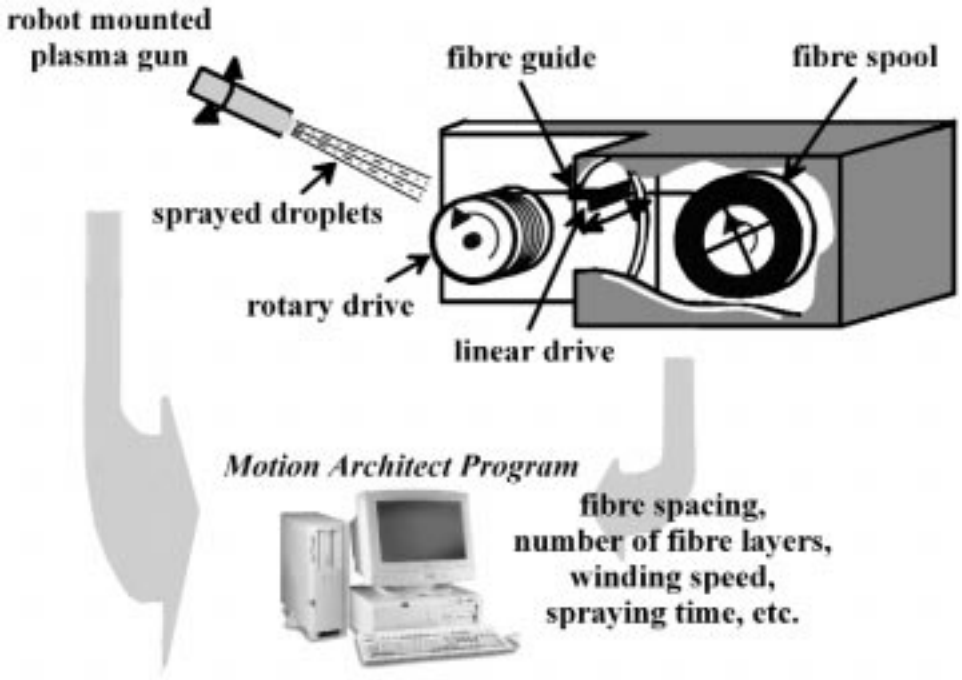

Fig. 1 Schematic diagram of spray/wind process that combines LPPS and concurrent fiber winding for manufacture of a multilayer composite ring

SiAlON powders using a V-shaped blender rotating for 48 h. SiAlON is a solid solution of Si_3N_4 with Al_2O_3 and AlN. The particle size of the mixture was in the range of 10 to 40 μm, which was suitable for LPPS. Sigma 1140+ SiC fiber (108 μm diameter) from the Defence Evaluation and Research Agency (DERA, Farnborough, United Kingdom) was used as the reinforcement. The fiber was manufactured by chemical vapor deposition of β-SiC onto a 14 μm diameter W core and had an outer graphitic C coating of $\sim$5 μm thickness.

SCS-6 (142 μm diameter) and SCS-9 (78 μm diameter) SiC fibers from Avco-Textron (Lowell, MA) have been widely investigated for metal matrix composites and consist of a SiC sheath surrounding a C-core and have an outer C-rich coating of $\sim$3 μm. In this study, matrix-cracking stresses in $MoSi_2$ based composites were calculated for reinforcing with SCS-6 and SCS-9 SiC fibers and were compared with those for $MoSi_2$ based composites reinforced with 1140+ SiC fiber.

2.2 Optimization of LPPS Parameters

The LPPS optimization for the SiAlON-$MoSi_2$ powder was performed using a two-level, eight-run experimental design approach.[10] This approach is used to provide an initial set of optimized parameters and to expose the most influential LPPS parameters on the critical matrix characteristics, such as porosity.[11,12] The LPPS was performed using a Sulzer Metco A2000 plasma spray unit (Switzerland), with Ar primary plasma gas and H_2 secondary gas. The five most influential LPPS parameters were selected as gun current, primary and secondary plasma gas flow rate, chamber pressure, and spray distance. The initial low and high values for each parameter are shown in Table 1. Other LPPS parameters were fixed: for example, powder feed rate of 0.58 g/s, powder carrier gas flow rate of 1.6 l/min, and five spraying passes at a gun speed of 100 mm/s. An Al_2O_3 grit-blasted stainless steel disc of 25 mm diameter was used as the substrate for parameter optimization. For each set of LPPS parameters, porosity (area fraction) and thickness of the deposits were determined using an optical microscopy with an image analysis software, and surface roughness was measured by a Rank Taylor-Hobson profilometer (Supersonic 3+) in which a sharp diamond stylus travels over the sample surface.

Table 1 Experimental design for LPPS

Run	Gun current (A)	Ar flow rate (l/min)	H_2 flow rate (l/min)	Chamber pressure (mbar)	Spray distance (mm)
1	700	35	4	200	300
2	700	35	8	200	270
3	700	45	4	80	300
4	700	45	8	80	270
5	800	35	4	80	270
6	800	35	8	80	300
7	800	45	4	200	270
8	800	45	8	200	300

2.3 Manufacture of Multilayer Composites

Spray/wind processing combines concurrent fiber winding and LPPS to manufacture multilayer fiber reinforced composite rings. Concurrent fiber winding is performed using a specially designed and constructed apparatus, which is schematically shown in Fig. 1. A mild, steel cylindrical substrate of 160 mm diameter and 100 mm width is mounted onto a rotary drive, and a fiber guide is attached to a linear drive. A single fiber supplied

from a prewound fiber spool is threaded through the fiber guide and fixed onto the cylinder. The fiber guide reciprocates back and forth along the cylinder axis, and the relative speed of reciprocating motion to rotating motion controls the fiber spacing. The reciprocating motion of the linear drive and the winding motion of the rotary drive are synchronized by Motion Architect software (Parker Hannifin Co., Cleveland, OH), which is programmed offline. This software is also interfaced to the software controlling the motion of the LPPS five-axis robot so that the desired fiber arrangement and fiber volume fraction can be preprogrammed and achieved reproducibly.

At the beginning of a spray/wind procedure, the plasma gun moves quickly to a spraying position perpendicular to the cylinder surface at a distance of 270 mm. Liquid, desirably, and a small fraction of solid and partially melted droplets are then sprayed onto the rotating cylinder to form an initial matrix layer during concurrent fiber winding. After the programmed matrix thickness is achieved, the powder spraying is halted by the LPPS and Motion Architect software, and the plasma gun is moved to a safe position far away from the fiber winding system. Meanwhile, the fiber winding continues onto the matrix layer with a predetermined fiber spacing and preset number of revolutions. Spraying is recommenced onto the fiber wound surface to bind the fiber into a composite preform. Alternate fiber winding and matrix spraying operations continuously build up the composite layer. The deposit/substrate temperature during spray/wind was measured by attaching a small K-type thermocouple on the substrate surface and monitoring the temperature as a function of time using a datalogger.

Four-layer SiC fiber reinforced $MoSi_2$ and SiAlON-$MoSi_2$ rings with a center-to-center fiber spacing of 300 μm were manufactured using optimized LPPS parameters from the experimental design study. The spray/wind $MoSi_2$ based composites were cut using a plasma cutter and removed from the mild steel substrate by immersing in 10% H_2SO_4 for 2 h, with no effect on the $MoSi_2$ based matrices or SiC fibers. In order to simulate the generation of residual stresses expected during a secondary consolidation cycle, samples were subjected to a high-temperature isothermal heat treatment in an N_2 atmosphere furnace at 1500 °C for 1 h, heated and cooled at 3 °C/min.

Microstructural examination used optical and scanning electron microscopy (SEM) on polished cross-section samples of SiC_f/SiAlON-$MoSi_2$ composite. X-ray mapping was used to characterize the elemental distribution around the fiber-matrix interface; and it was performed on a dedicated analytical electron probe microanalyzer.

3. Results and Discussion

3.1 Optimization of LPPS for Matrix Deposit

The porosity, surface roughness, and thickness of SiAlON-$MoSi_2$ deposits for each of the experimental conditions in Table 1 are shown in Table 2. Note that no deposit was produced for runs 3, 4, and 5, which then limited the subsequent experimental design analysis. The porosity and surface roughness were not strongly affected by LPPS parameters, although variations in deposit thickness (deposit efficiency) were marked, ranging from 275 to 490 μm. Using the available reduced data set, an average "response" of the deposit thickness

Table 2 Porosity, surface roughness, and thickness of LPPS SiAlON-$MoSi_2$ deposits

Run	Porosity (%)	Surface roughness (μm)	Thickness (μm)
1	2.8	7.8	240
2	1.0	4.8	490
3	n/a	n/a	n/a
4	n/a	n/a	n/a
5	n/a	n/a	n/a
6	2.3	4.2	335
7	2.3	4.6	275
8	1.1	4.5	310

Table 3 Average response for each parameter on deposit thickness

Level	Gun current	Ar flow rate	H_2 flow rate	Chamber pressure	Spray distance
Low (1)	182	266	128	83	191
High (2)	230	146	283	328	221
Difference, (2)-(1)	48	**−120**	**155**	**245**	30

for each parameter was calculated. For example, in the case of Ar flow rate, the relative effects of low and high Ar flow rate on deposit thickness can be obtained by subtracting the average for those experiments, using low Ar flow rate (run numbers 1, 2, 5, and 6) from the average using high Ar flow rate (run numbers 3, 4, 7, and 8). These differences of high and low averages are given in Table 3. In this case, an increase in the Ar flow rate from 35 to 45 l/min gave a decrease in the average response of the thickness. The greater the difference between average thickness at low and high levels, the more influential that LPPS parameter is on subsequent deposit thickness. The most important LPPS parameters affecting deposit thickness are Ar flow rate, H_2 flow rate and chamber pressure, which are shown in bold type in Table 3. An increase in Ar flow rate gave a thinner deposit (low deposition efficiency). The cooling effect of excessive plasma gas reduced plasma enthalpy per unit volume, and particle melting became more inefficient. In contrast, a small increase in secondary H_2 flow rate increased thickness because the increased gas volume was more than offset by the large increase in plasma enthalpy and thermal conductivity.[13] A lower chamber pressure gave a thinner deposit because the plasma hot zone was narrower and lengthened, and gas and particle velocities were increased. This made it difficult to accurately inject the feedstock particles into the highest temperature region of the plasma, and the dwell time of particles in this region was relatively short. The predicted optimum LPPS parameters were current of 800 A, Ar flow rate of 35 l/min, H_2 flow rate of 8 l/min, chamber pressure of 200 mbar, and spray distance of 300 mm. A confirmation LPPS experiment was performed using these parameters, and the resultant deposit thickness was ~490 μm, similar to run 2 in the experimental design.

Further increases in the deposit thickness were sought to (a) maximize the utility of limited feedstock powder and (b) reduce processing times, hence, processing temperature and fiber dam-

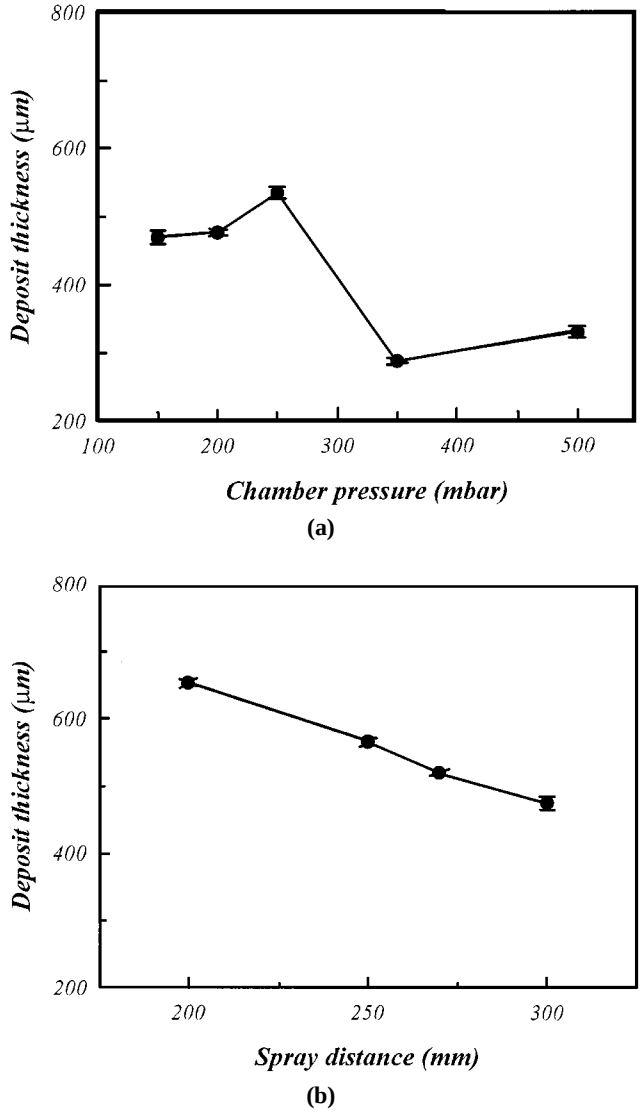

Fig. 2 Deposit thickness of LPPS SiAlON-$MoSi_2$ deposits as a function of (**a**) chamber pressure and (**b**) spray distance

age. A gun current of 800 A and H_2 flow rate of 8 l/min gave a plasma power of ~55 kW, which is close to the maximum operation power to maintain reasonable plasma anode and cathode life times. Therefore, changes in chamber pressure only were then pursued to increase deposition efficiency. Figure 2(a) shows a plot of deposit thickness against chamber pressure for SiAlON/$MoSi_2$. A maximum deposit thickness of ~580 μm was achieved at a chamber pressure of 250 mbar. Chamber pressures at and above 350 mbar led to a sharp decrease in deposit thickness. Although higher chamber pressure increased convective heat transfer and slowed particles in the plasma hottest regions, the flame became very short and broad at 350 mbar. It may have been possible to reoptimize all other LPPS parameters to preserve or improve deposition efficiency, but this was not pursued. Furthermore, at higher pressure, LPPS becomes more akin to APS with lower deposition velocities and corresponding higher porosity and surface roughness. Thus, the combination of chamber pressure and spray distance should be controlled to achieve a thicker deposit. Figure 2(b) shows the variation of deposit thickness as a function of spray distance at a chamber pressure of 250 mbar. The deposit thickness increased linearly with decreasing spray distance, as expected. However, a short spray distance led to a significant increase in deposit/substrate temperature: for example, at 200 mm, the temperature reached ~1300 °C. The premixed feedstock powder of SiAlON-$MoSi_2$ was then sprayed onto a fiber wound steel cylinder to manufacture a monotape, as a function of variation in the spray distance. A shorter spray distance had the advantage of high deposition efficiency, but spraying at <270 mm caused fiber failure as a result of an excessive increase in preform temperature and the impact of higher temperature melted and unmelted particles traveling at higher velocities. Consequently, optimum LPPS parameters for SiC_f/SiAlON-$MoSi_2$ were taken as current of 800 A, Ar flow rate of 35 l/min, H_2 flow rate of 8 l/min, chamber pressure of 250 mbar, and spray distance of 270 mm.

3.2 Microstructure of SiC_f/SiAlON-$MoSi_2$

Figure 3(a) shows the as-sprayed microstructure of a resulting monolithic SiAlON-$MoSi_2$ deposit. The SiAlON (dark phase) was uniformly and discontinuously distributed throughout the $MoSi_2$ (light phase). Both phases appeared as splats without any significant intermixing at splat boundaries, which was attributed to particle spreading of individual liquid droplets on impact and subsequent rapid solidification. The measured volume fraction of SiAlON was approximately 35 to 40%, similar to the initial premixed feedstock material and suggested no preferential loss of SiAlON or $MoSi_2$ during LPPS. Figure 3(b) is a high magnification SEM micrograph of fully consolidated SiAlON-$MoSi_2$ at 1500 °C, showing no significant reaction between $MoSi_2$ and SiAlON. Although there was a large difference of CTE between $MoSi_2$ and SiAlON, the small particle size prevented thermally induced microcracking.

The LPPS manufacture of fiber reinforced composites requires that the sprayed particles are molten at the point of deposition and have sufficient momentum to infiltrate between the fibers. Figure 4 shows the preform temperature history during the manufacture of a single-layer 1140+ SiC_f/SiAlON-$MoSi_2$ ring where preform temperature was measured by attaching a small thermocouple on the substrate surface. Periodic temperature variations occurred at any given point on the preform surface as it moved in and out of the spray because of the substrate rotation and plasma gun scanning. The temperature increased rapidly from room temperature at the start of spraying and reached ~600 °C at the end of spraying after 70 s. Figure 5(a) shows the cross-section microstructure of a four-layer 1140+ SiC_f/SiAlON-$MoSi_2$ composite. The microstructure showed good matrix infiltration between the fibers and, generally, a well-controlled fiber spacing. The majority of pores were located in the fiber shadows, with a size of a few tens of micrometers, because the fiber was wound against an undulating sprayed surface.[14] Debonding between first and second layers occurred during removal of the preform from the cylinder substrate, because the relatively low temperature of manufacture (<600 °C) resulted in insufficient bonding between the previous and new sprayed layer. Subsequent hot pressing at 1500 °C promoted the diffusion bonding of the matrix and the closure of the micro-

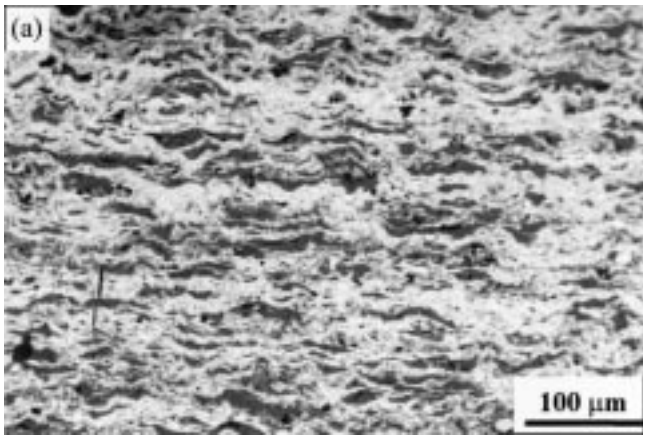

(a)

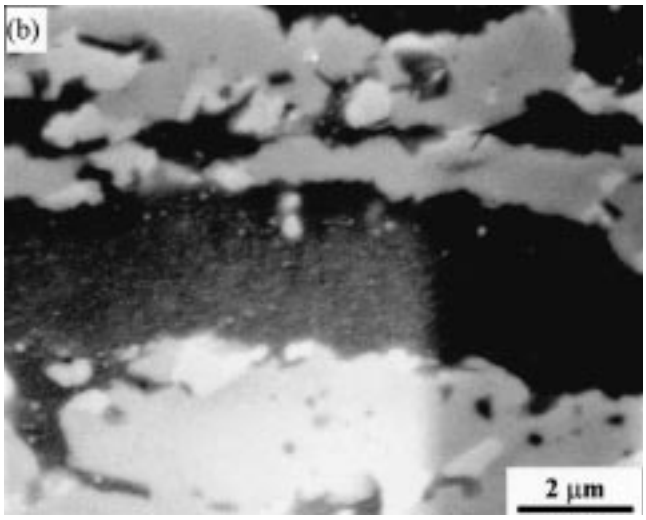

(b)

Fig. 3 Microstructure of SiAlON(40 vol.%)-$MoSi_2$ deposit: (**a**) as-sprayed, showing uniform distribution of SiAlON (dark phase) through $MoSi_2$ (light phase); and (**b**) consolidated at 1500 °C, showing no microcracking and chemical reaction between SiAlON and $MoSi_2$

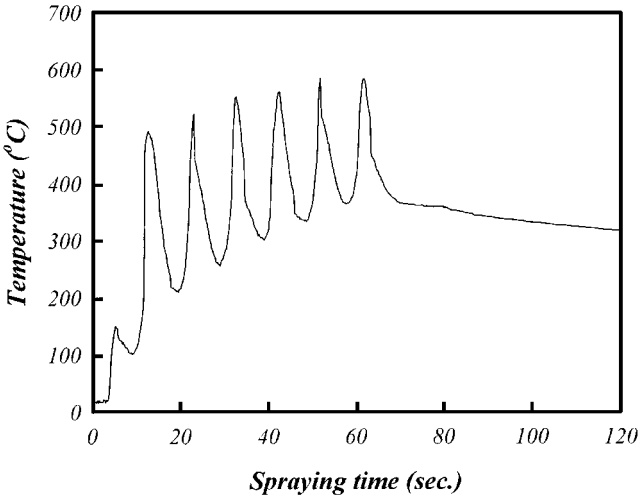

Fig. 4 Temperature variation of deposit/substrate preform during the manufacture of single-layer $MoSi_2$ based composite ring

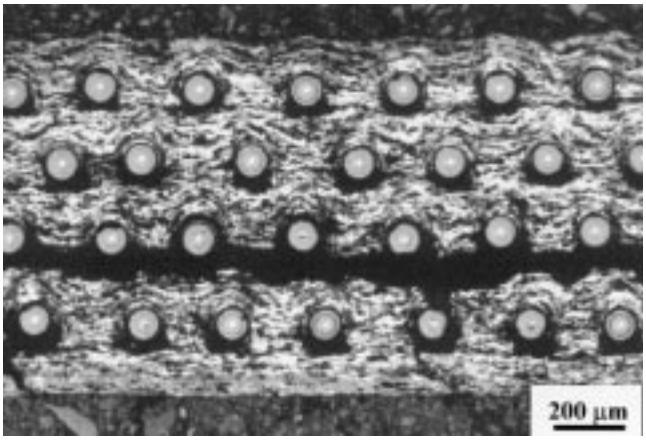

Fig. 5 Optical micrograph of four-layer 1140+ SiC_f/SiAlON-$MoSi_2$, showing a good fiber distribution. Note that composite layer debonding between first and second layers (indicated by dashed line) occurred during sample preparation

pores between splats and in fiber shadows. Matrix cracking behavior of the composites will be discussed in Section 3.3.

Figure 6(a) shows the interface microstructure of 1140+ SiC_f/$MoSi_2$ exposed at 1500 °C for 1 h. A thick interfacial reaction layer of 3 to 5 μm was formed by consumption of the C coating. The base SiC fiber is thermodynamically compatible with $MoSi_2$,[1] but the outer C coating readily reacts with the $MoSi_2$ based matrix to form SiC during high temperature exposure. Figures 6(b) through (d) are electron probe microanalyzer (EPMA) elemental X-ray maps of the resulting interfacial reaction zone for Mo, Si, and C, respectively, showing that the reaction zone was relatively enriched in Mo and lower in Si compared with the $MoSi_2$ matrix. Singh and Bose[15] suggested the reaction between C and $MoSi_2$ as

$$C(s) + \frac{1}{2}MoSi_2(s) = \frac{1}{2}Mo(s) + SiC(s) \qquad \text{(Eq 1)}$$

The Gibbs free energy change for this reaction is negative at temperatures of 1300 to 1900 °C, indicating that the C/$MoSi_2$ system is unstable at the heat treatment temperature of 1500 °C. However, Costa e Silva and Kaufman suggested that Mo_5Si_3 and Mo_5Si_3C might also be formed.[16] Any interfacial reaction will influence the interface bond strength and, consequently, the tendency to debond at the fiber-matrix interface. For brittle matrix composites, a relatively weak fiber-matrix bond is desirable in order to enhance fracture toughness by promoting energy absorbing delamination and fiber pullout.[17] Current commercial DERA Sigma and Textron SiC fibers both employ an outer C based coating, which will lead to the formation of interfacial reaction layers. Bhatti *et al.*[18] exploited the stability of SiC with $MoSi_2$ using an SCS-9 fiber with standard C-rich outer coating but then added a further SiC coating. In this way, fiber protection and toughening was provided by the C layer as in standard Textron SCS fibers, while the additional SiC protected the C from excessive reaction with the $MoSi_2$ based matrix. Further

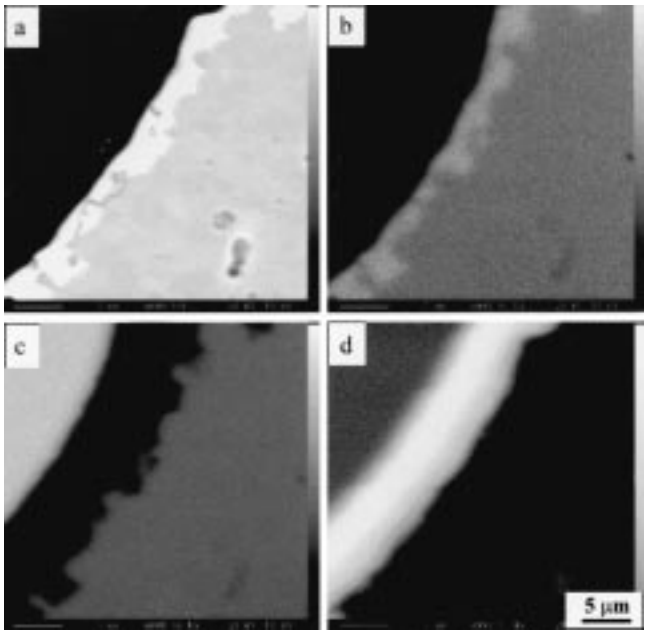

Fig. 6 EPMA elemental maps of heat-treated 1140+ $SiC_f/MoSi_2$ at 1500 °C for 1 h: (**a**) backscattered electron image, (**b**) Mo, (**c**) Si, and (**d**) C

study on the effects of a SiC barrier outer coating on interfacial reaction and toughening is in progress.

3.3 Residual Stresses and Matrix Cracking

The CTE mismatch between the matrix and the fiber induces stresses in both the fiber and matrix during cooling after manufacture. Assuming the material is stress free at the manufacturing temperature, residual stresses are compressive in the fiber and tensile in the matrix. Assuming that the constituents remain elastic, the axial residual stress, σ_z, in the fiber and matrix are[19]

$$\sigma_z^f = \frac{\lambda_2}{\lambda_1}\frac{E_f}{E_c}\frac{(1-f)E_m}{1-\nu_m}\Omega \quad \text{(Eq 2)}$$

$$\Omega = (\alpha_f - \alpha_m)\Delta T \quad \text{(Eq 3)}$$

with

$$\sigma_z^m = -\frac{f}{(1-f)}\sigma_z^f \quad \text{(Eq 4)}$$

where E_i is the Young's modulus; Ω is the thermally induced mismatch strain between matrix and fiber; α_i is the CTE; ΔT is the temperature difference between manufacture temperature (1500 °C) and room temperature; ν_m is the matrix Poisson's ratio; f is the fiber volume fraction; λ_1 and λ_2 are coefficients that depend on the elastic constants; and the script $i = f, m,$ and c refers to fiber, matrix, and composite, respectively. The circumferential σ_θ^f and radial σ_r^f stresses in the fiber are[19]

$$\sigma_\theta^f = \sigma_r^f = -\frac{E_m}{2\lambda_1}\frac{1-f}{1-V_m}\Omega \quad \text{(Eq 5)}$$

Table 4 Calculated residual stresses after cooling from 1500 to 25 °C

(MPa)	SiC_f(15 vol.%)/ $MoSi_2$	SiC_f(15 vol.%)/ SiAlON(40 vol.%)-$MoSi_2$
$\sigma_\theta^f = \sigma_r^f$	−1331	−692
σ_z^f	−2721	−1384
σ_z^m	480	244

The CTE value of SiAlON-$MoSi_2$ can be estimated using the following relationship:[20]

$$\alpha = \alpha_{MoSi_2} - \frac{(\alpha_{MoSi_2} - \alpha_{SiAlON})}{\left(1 + \frac{V_{MoSi_2}}{V_{SiAlON}}\frac{E_{MoSi_2}}{E_{SiAlON}}\right)} \quad \text{(Eq 6)}$$

where α is the CTE, 8.3×10^{-6}/ °C for $MoSi_2$ and 3.5×10^{-6}/ °C for SiAlON; V is the volume fraction, 0.6 for $MoSi_2$ and 0.4 for SiAlON; and E is the elastic modulus, 380 GPa for $MoSi_2$ and 300 GPa for SiAlON.[21] The estimated CTE for SiAlON (40 vol.%)-$MoSi_2$ is consequently 6.6×10^{-6}/ °C. The calculated residual stresses for $SiC_f/MoSi_2$ and SiC_f/SiAlON(40 vol.%)-$MoSi_2$ following heat treatment at 1500 °C are listed in Table 4, where f is 0.15 and ΔT is 1475 °C. Table 4 shows that matrix and fiber residual stresses are lower for SiAlON(40 vol.%)-$MoSi_2$ than for $MoSi_2$. The residual compressive (clamping) stresses at the interface increase sliding resistance, and the corresponding tensile residual stress in the brittle matrix will promote early cracking.

Matrix cracking originates from flaws under a combination of applied external stresses and residual stresses. For debonding interfaces, the steady-state cracking stress, σ_c, for a crack normal to fiber axis is[19]

$$\sigma_c = \left(\frac{6G_m\tau E_f^2 E_c^2 f^2}{RE_m^2(1-f)}\right)^{1/3} - \frac{E_c\sigma_z^m}{E_m} \quad \text{(Eq 7)}$$

where G_m is the fracture energy of $MoSi_2$ matrix, assumed as ~0.15 kJ/m^2,[22] τ is the sliding resistance of the debonded interface, and R is the fiber diameter. The first term on the right-hand side of Eq 7 represents the material resistance to crack propagation, which increases with increasing the interface area of fiber-matrix and the interface sliding resistance. In the case of residual compression at the interface, the sliding resistance can be expressed as[22]

$$\tau = \tau_0 - \mu\sigma_r^f, \quad \sigma_r^f < 0 \quad \text{(Eq 8)}$$

where μ is the friction coefficient ≈0.18,[22] and τ_0 is the sliding resistance when the normal residual stress at the interface becomes positive. The value of τ_0 is difficult to measure, but a typical value of τ_0 is reported as ~20 MPa, assuming that no interfacial reactions occur.[22] In this study, it was assumed that despite evidence of interfacial reactions, τ_0 = 20 MPa so that $\mu\sigma_r^f >> \tau_0$. Further work is required to determine the true value of τ_0 and is beyond the scope of this study. When the last term

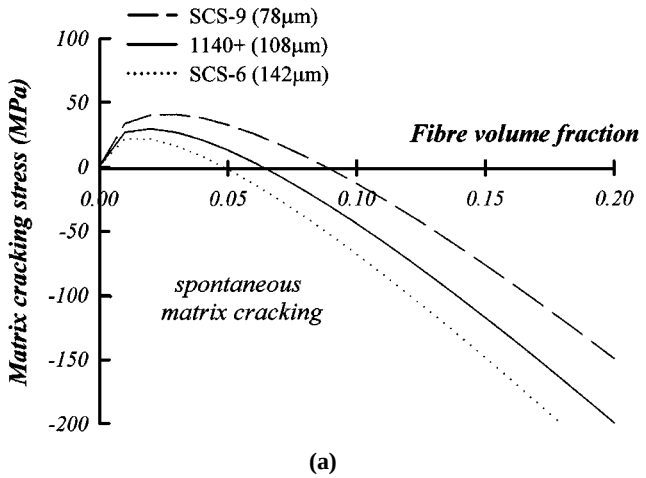

(a)

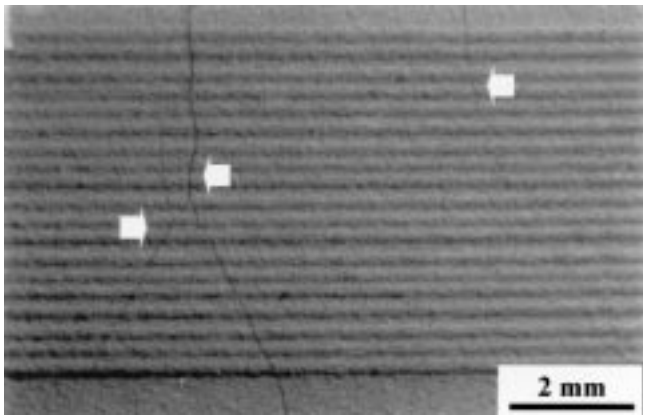

(b)

Fig. 7 (**a**) Matrix cracking stress of $SiC/MoSi_2$ as a function of fiber volume fraction and fiber diameter and (**b**) several matrix cracks in 1140+ SiC_f (15 vol.%)/$MoSi_2$ after cooling from 1500 to 25 °C at 3 °C/min

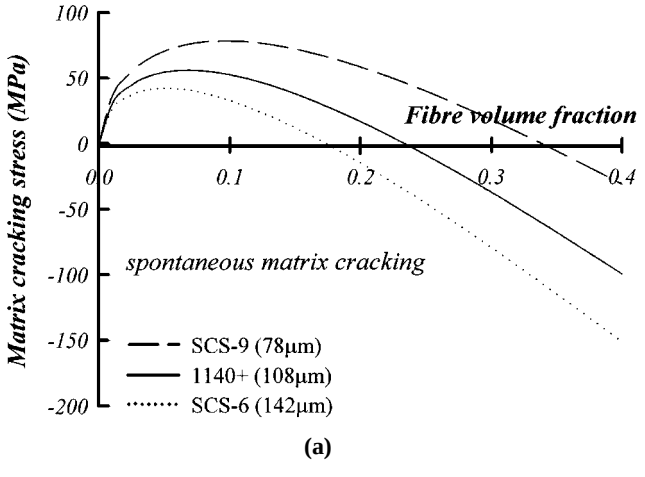

(a)

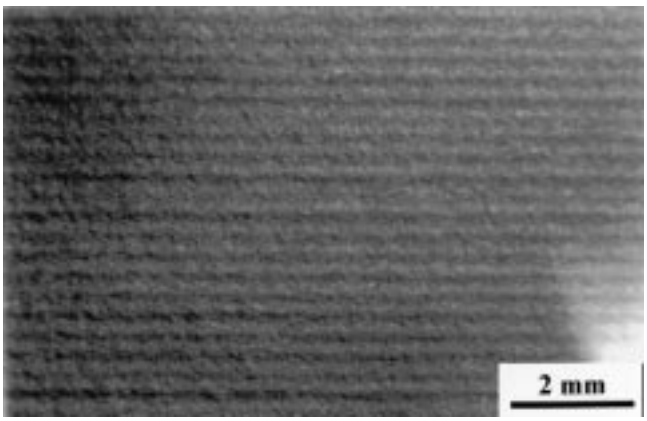

(b)

Fig. 8 (**a**) Matrix cracking stress of SiC_f/SiAlON(40 vol.%)-$MoSi_2$ and (**b**) avoidance of matrix cracks in 1140+ SiC_f (15 vol.%)/SiAlON (40 vol.%)-$MoSi_2$ after cooling from 1500 to 25 °C at 3 °C/min

on the right-hand side of Eq 7 is relatively large compared with the crack propagation resistance term, σ_c becomes negative, with the physical implication that steady-state matrix cracks propagate spontaneously under residual stresses.

Figure 7(a) shows the calculated matrix cracking stress in 1140+ (108 μm diameter), SCS-9 (78 μm), and SCS-6 (142 μm) $SiC_f/MoSi_2$ as a function of fiber volume fraction for Eq 7. Depending on fiber diameter, the maximum stress required for matrix cracking occurs at a fiber volume fraction of 2 to 3%, and, in general, greater stresses for matrix cracking are required as the fiber diameter decreases. As the fiber volume fraction increases further, the matrix cracking stress reduces and eventually becomes negative, implying spontaneous matrix cracking. For 1140+ SiC fiber, matrix cracking occurs with only 6% fiber volume fraction. Experimentally, on cooling from 1500 to 25 °C at 3 °C/min, 1140+ SiC_f (15 vol.%)/$MoSi_2$ showed several matrix cracks perpendicular to the fiber axis, indicated by arrows in Fig. 7(b).

The matrix-cracking stress was similarly calculated for SiC_f/SiAlON(40 vol.%)-$MoSi_2$, as shown in Fig. 8(a). As intended, the SiAlON-$MoSi_2$ matrix leads to an overall increase in the stresses required for matrix cracking and extends the permissible fiber volume fraction, for example, up to 23% for 1140+ and 35% for SCS-9. This result derives in part from the reduced tensile residual stress in the matrix, as shown in Table 4. Figure 8(b) shows the surface of an 1140+ SiC_f (15 vol.%)/SiAlON(40 vol.%)-$MoSi_2$ heat treated at 1500 °C and cooled down to room temperature. Unlike Fig. 6(b) for unalloyed $MoSi_2$ matrix, no matrix cracking is evident. Given the uncertainty in some of the thermophysical properties of the materials, theoretical predictions for spontaneous matrix cracking are in broad agreement with experimental findings.

4. Conclusions

1. The LPPS parameters for SiAlON-$MoSi_2$ powder were optimized by a two-level experimental design method followed by further optimization, which provided a relatively smooth sprayed surface, low matrix porosity, and best deposition efficiency.

2. The SiAlON-$MoSi_2$ deposits were characterized by a lamellar structure built up of individual splats resulting from rapid solidification, and there was a uniform distribution of

SiAlON splats throughout the $MoSi_2$ matrix. Four-layer SiC fiber reinforced $MoSi_2$ based composite rings were successfully manufactured by spray/wind and had a regular fiber distribution and low porosity of $<2\%$. High temperature consolidation of the composite led to the formation of a thick reaction zone at the fiber-matrix interface by consumption of the outer C coating on 1140+ SiC fiber, and there was no evidence of reaction between SiAlON and $MoSi_2$.

3. Matrix cracking occurred in 1140+ SiC_f(15 vol.%)/$MoSi_2$ after heat treatment at 1500 °C and was attributed to the large tensile residual stresses in the matrix developed on cooling because of CTE mismatch between $MoSi_2$ and SiC. The addition of 40 vol.% SiAlON into the $MoSi_2$ matrix effectively eliminated the matrix cracking because of improved matrix-fiber CTE matching and reduced residual tensile stresses. The maximum permissible fiber volume fraction to avoid matrix cracking was 6% for 1140+ SiC/$MoSi_2$ and 23% for 1140+ SiC_f/SiAlON (40 vol.%)-$MoSi_2$.

Acknowledgment

The authors thank The Royal Society and Defence Evaluation and Research Agency for financial support.

References

1. P.J. Meschter and D.S. Schwartz: *J. Met.*, 1989, vol. 41 (10), pp. 52-55.
2. A.K. Vasudevan and J.J. Petrovic: *Mater. Sci. Eng.*, 1992, vol. A155 (1–2), pp. 1-17.
3. R.G. Castro, R.W. Smith, A.D. Rollett, and P.W. Stanek: *Mater. Sci. Eng.*, 1992, vol. A155 (1–2), pp. 101-07.
4. J.J. Petrovic and R.E. Honnel: *J. Mater. Sci.*, 1990, vol. 25 (10), pp. 4453-56.
5. W. Soboyejo, F. Ye, and D.S. Schwartz: *Metall. Mater. Trans. A*, 1995, vol. 26A (9), pp. 2263-73.
6. D.E. Alman, N.S. Stoloff, A. Bose, and R.M. German: *J. Mater. Sci.*, 1995, vol. 30 (20), pp. 5251-59.
7. M.G. Hebsur: *Mater. Sci. Eng.*, 1999, vol. A261 (1–2), pp. 24-33.
8. A.M. Baker, P.S. Grant, R. Castro, and H. Kung: *Mater. Sci. Eng.*, 1999, vol. A261 (1–2), pp. 196-203.
9. C. Huang, C. Yuh, M. Farooque, D. Zhu, Y. Xu, and W.M. Kriven: *J. Am. Ceram. Soc.*, 1997, vol. 80 (11), pp. 2837-44.
10. N. Belavendram: *Quality by Design*, Prentice-Hall, London, 1995.
11. K.H. Baik and P.S. Grant: in *Materials, Functionality & Design, Vol. 1: Metals and Composites*, L.A.J.I. Sarton and H.B. Zeedijk, eds., FEMS, Netherlands Society for Materials Science, Netherlands, 1997, pp. 341-46.
12. K.H. Baik and P.S. Grant: in *Thermal Spray: Meeting the Challenges of the 21st Century*, C. Coddet, ed., ASM International, Materials Park, OH, 1998, pp. 1193-98.
13. D. Matejka and B. Benko: *Plasma Spraying of Metallic and Ceramic Materials*, John Wiley & Sons, New York, NY, 1989.
14. K.H. Baik and P.S. Grant: *Mater. Sci. Eng.*, 1999, vol. A265 (1–2), pp. 77-86.
15. M. Singh and A. Bose: in *Processing and Fabrication of Advanced Materials for High Temperature Applications*, V.A. Ravi and T.S. Srivatsan, eds., TMS, Warrendele, PA, 1992, pp. 157-72.
16. A. Costa e Silva and M.J. Kaufman: *Mater. Sci. Eng.*, 1995, vol. A195 (1–2), pp. 75-88.
17. C.M. Ward-Close, R. Minor, and P.J. Doorbar: *Intermetallics*, 1996, vol. 4, pp. 217-29.
18. A.R. Bhatti: "*Processing and Characterisation of SiC Fiber Reinforced $MoSi_2$ Based Composites*," DERA/SMC/SM2/CR980083/1.0, DERA, Farnborough, United Kingdom, 1998.
19. A. Budiansky, J.W. Hutchinson, and A.G. Evans: *J. Mech. Phys. Solids*, 1986, vol. 34 (2), pp. 167-83.
20. M. Smagorinski, P. Tsantrizos, S. Grenier, and M. Entezarian: *J. Met.*, 1996, vol. 48 (8), pp. 56-58.
21. X. Jiang, Y. Baek, S. Lee, and S. Kang: *J. Am. Ceram. Soc.*, 1998, vol. 81 (7), pp. 1907-12.
22. H.E. Deve and M.J. Maloney: *Acta Metall. Mater.*, 1991, vol. 39 (10), pp. 2275-84.